Behavioral/Systems/Cognitive

Laminar and Columnar Organization of Ascending Excitatory Projections to Layer 2/3 Pyramidal Neurons in Rat Barrel Cortex

Gordon M. G. Shepherd and Karel Svoboda

Howard Hughes Medical Institute, Cold Spring Harbor Laboratory, Cold Spring Harbor, New York 11724

Excitatory synaptic projections to layer 2/3 (L2/3) pyramidal neurons in brain slices from the rat barrel cortex were measured using quantitative laser-scanning photostimulation (LSPS) mapping. In the barrel cortex, cytoarchitectonic "barrels" and "septa" in L4 define a stereotypical array of landmarks, allowing alignment and averaging of LSPS maps from multiple cells in different slices. We distinguished inputs to L2 and L3 neurons above barrels and septa. Average input maps revealed that barrel-related ascending projections (L4→2/3 ^{barrel}) interdigitated with a novel septum-related projection (L5A→2 ^{septum}). We also explored the functional organization of these projections by comparing the input maps of multiple cells in individual slices. L2/3 cells sharing the same barrel-related column showed strong correlations in their input maps, independent of their precise locations within the column; otherwise, correlations fell rapidly as a function of intersomatic separation. Our data indicate that barrel-related and septum-related columns are associated with distinct functional circuits. These projections are likely to mediate parallel processing of somatosensory signals within the barrel cortex, with L4→2/3 ^{barrel} and L5A→2 ^{septum} representing the intracortical continuations of, respectively, the subcortical lemniscal and paralemniscal systems conveying somatosensory information to the barrel cortex.

Key words: barrel; cortex; septum; paralemniscal; somatosensory; microcircuit; photostimulation; glutamate uncaging; connectivity

Introduction

In the rodent somatosensory barrel cortex, layer 2/3 (L2/3) pyramidal neurons are of particular interest both because they participate in the L4→2/3 pathway and therefore are key components in some of the earliest stages of intracortical processing of the vibrissal somatosensory signals (Simons, 1978; Armstrong-James and Fox, 1987; Armstrong-James et al., 1992; Ahissar et al., 2000; Brecht et al., 2003; for review, see Armstrong-James, 1995) and because they exhibit robust experience-dependent plasticity (Fox, 1992; Diamond et al., 1994; Feldman, 2000; Lendvai et al., 2000; Stern et al., 2001; Allen et al., 2003; Shepherd et al., 2003) (for review, see Fox, 2002; Foeller and Feldman, 2004).

The barrel-related L4→2/3 (L4→2/3 ^{barrel}) pathway is considered a "canonical" cortical columnar circuit: a major, basic projection readily detected with a variety of techniques. Originally elucidated by *in vivo* recordings (for review, see Armstrong-James, 1995), it has been studied extensively *in vitro* both anatomically and physiologically (Petersen and Sakmann, 2001; Feldmeyer et al., 2002; Bender et al., 2003; Lübke et al., 2003; Shepherd et al., 2003; Bureau et al., 2004; Staiger et al., 2004).

Between L4 barrels are septa (Woolsey and Van der Loos, 1970; Rice, 1995). Cells in septa and septum-related columns are associated with distinct thalamocortical (Koralek et al., 1988; Chmielowska et al., 1989; Lu and Lin, 1992) and intracortical (Kim and Ebner, 1999; Shepherd et al., 2003) circuits and display different receptive-field properties compared with barrel-related cells (Brecht and Sakmann, 2002; Brecht et al., 2003).

Because barrels and septa demarcate barrel- and septum-related cortical columns spanning the vertical extent of the cortex, these cytoarchitectonic features allow one to align, average, and compare measurements from different brain slices and animals. In previous studies of juvenile rats (Shepherd et al., 2003; Bureau et al., 2004), we examined the spatial organization of synaptic inputs to L2/3 cells in the barrel cortex using laser-scanning photostimulation (LSPS), a tool that allows mapping of functional synaptic connections that converge onto single neurons (Callaway and Katz, 1993; Katz and Dalva, 1994; Schubert et al., 2001; Shepherd et al., 2003). On average, L2/3 ^{barrel} cells received prominent translaminar inputs from the subjacent barrel in L4; L2/3 ^{septum} cells had only one-half as much L4 input.

Here, we use LSPS to measure the strength of excitatory synaptic projections to L2/3 pyramidal neurons in the barrel cortex of young adult rats. To analyze these circuits, we average maps across multiple cells of the same positionally defined class to obtain a map of the population or canonical circuit (Shepherd et al., 2003; Bureau et al., 2004). In addition, to examine features in the individual maps that are lost in the averaging process, we also use a neighboring-neuron approach to record multiple input

maps for multiple neurons per slice and compare maps with correlation analysis. Our experiments identified a novel ascending projection in the neocortex, L5A→2 [septum], and revealed that this is organized in a parallel, interdigitating manner with L4→2/3 [barrel].

Materials and Methods

Slices. Sprague Dawley rats were used in accordance with institutional animal care guidelines. For most experiments, we used young adult rats at postnatal day 25 (P25) to P36. For pair-mapping experiments (see Fig. 4), we used juvenile to young adult animals (P13–P36). Animals were anesthetized and decapitated, and the brains were removed rapidly and transferred to a chilled cutting solution composed of the following (in mM): 110 choline chloride, 25 $NaHCO_3$, 25 D-glucose, 11.6 sodium ascorbate, 7 $MgSO_4$, 3.1 sodium pyruvate, 2.5 KCl, 1.25 NaH_2PO_4, and 0.5 $CaCl_2$. Brain slices were cut across the barrel rows (Finnerty et al., 1999). Slices were cut at a thickness of 300 μm, representing a favorable compromise between opposing aims: although thicker slices may preserve more structural and functional circuitry, thinner slices offer better bright-field imaging of cytoarchitectonic landmarks and contain more homogeneous circuitry in the *z*-axis (e.g., in thicker slices, what appears to be a barrel region may actually also harbor some septum somewhere along the *z*-axis). Slices were transferred to artificial CSF (ACSF) consisting of the following (in mM): 127 NaCl, 25 $NaHCO_3$, 25 D-glucose, 2.5 KCl, 4 $MgCl_2$, 4 $CaCl_2$, and 1.25 NaH_2PO_4, aerated with 95% O_2/5% CO_2. Slices in ACSF were first incubated at 34°C for ~30 min, then maintained at room temperature before use. For recording, slices were transferred to the recording chamber, oriented in the standard recording configuration (see below), and stabilized by an arc of gold wire. Under higher magnification, apical dendrites of infragranular pyramidal neurons were inspected to verify that they ran parallel to the plane of the slice.

UV source. A frequency-tripled Nd:YVO₄ laser (model 3501; DPSS Lasers, Santa Clara, CA) provided excitation at 355 nm (see Fig. 1*ai*). The high repetition rate (100 kHz) and adequate power level (>0.5 W) of the laser provided high-efficiency uncaging with 1.0 ms flashes (100 pulses). Flash stimuli were generated by delivering a 1.0 ms pulse either as a logic signal to the Q-switch or, with the Q-switch on, as an analog signal to a Pockels cell (Conoptics, Danbury, CT). In addition, we blocked the low-intensity (~1% power) "bleed-through" beam (otherwise used for alignment) with a mechanical shutter (Uniblitz; Vincent Associates, Rochester, NY) that was programmed to open immediately (~1 ms) before the Q-switched UV flash and to close immediately after. The beam power was modulated by a neutral density gradient wheel (Edmund Industrial Optics, Barrington, NJ) and in some experiments also by a Pockels cell. Power was measured by diverting a small fraction of the beam with a glass coverslip to a photodiode (UDT Sensors, Hawthorne, CA). The photodiode signal was sampled with each trace and calibrated routinely against a laser power meter positioned at the back focal plane of the microscope. We measured the UV transmission of the objective lenses (e.g., ~70% for the 4× lens used for mapping). For each UV stimulus, we recorded the nominal power at the level of the specimen. Objective lenses were cleaned daily to remove any UV-attenuating salts.

Scan system. The scan system (see Fig. 1*aii*) comprised an *X–Y* pair of scan mirrors, scan lens, tube lens, and objective lens (Mainen et al., 1999; Tsai et al., 2002). The beam position was controlled by modulating the voltage signals to the mirror galvanometers (model 6210; Cambridge Technology, Cambridge, MA). Because the mirrors and the back aperture of the objective were in conjugate planes, deflections of the mirrors caused tilting of the beam around a stationary spot at the level of the back aperture of the objective, translating into scanning at the level of the specimen (image plane). The ~1.5-mm-diameter beam from the laser underfilled the scan mirrors. The mirrors directed the beam through a scan lens with focal length $f_{scan} = 100$ mm (UV grade fused silica plano-convex, 50.8 mm diameter, UV coated; Edmund Industrial Optics); the beam entered the microscope (BX51WI; Olympus, Tokyo, Japan) via a dichroic mirror (380DRLP; Chroma Technology, Brattleboro, VT) and was focused by a UV-transmitting tube lens with focal length $f_{tube} = 180$ mm (CVI Laser, Albuquerque, NM). These two lenses were configured as a Keplerian telescope (i.e., their separation $d_2 = f_{scan} + f_{tube}$. Then $d_1 = (f_{scan})^2/f_{tube} + f_{scan} - d_3(f_{scan}/f_{tube})^2$, where d_1 is the distance from the scan mirrors to the scan lens and d_3 is the separation between the tube lens and back aperture of the objective) (Tsai et al., 2002).

Beam expansion was limited to the 2× optical gain through the scan lens–tube lens pair, thus underfilling the back aperture of the microscope objective and minimizing the numerical aperture (NA) of the scanning beam. This was done to provide a more columnar (as opposed to conical) illuminating beam, keeping the mapping as two-dimensional as possible by reducing the axial resolution. In separate experiments, we measured the effective optical resolution by direct stimulation of glutamatergic responses across thin dendrites. Lateral (*XY*) resolution was ~15 μm, and axial (*Z*) resolution was >500 μm.

Positional calibration of the beam entailed coarse adjustment of the mirrors manually, and fine adjustment in software using offset factors, to center the beam. To move the beam, gain factors were empirically determined to move the mirrors with better than ~10 μm accuracy.

Perfusion system. We used a recirculating flow system to minimize bath volume and caged compound usage (see Fig. 1*aiii*). On the inflow side, 7.5 ml of ACSF was added to a reservoir manufactured from a 20 ml disposable pipette. The ACSF was carbogen bubbled within the reservoir and gravity-fed via thin tubing at a rate regulated by a standard intravenous drip regulator to the chamber. A peristaltic pump drove the outflow via thin tubing back to the reservoir.

Caged glutamate. Nitroindolinyl (NI)-caged glutamate (Canepari et al., 2001) (Sigma-RBI, St. Louis, MO) stock solution was prepared by dissolving 50 mg of NI-glutamate in distilled water and stored in 0.1 ml aliquots at −20°C for up to several weeks. An aliquot was added to the recirculating ACSF for a concentration of 0.37 mM. After 2–3 h of experimentation, the bath solution and NI-glutamate were refreshed. Care was taken to ensure a constant fluid level in the chamber of ~2.0–2.5 mm above the slice to avoid small fluctuations in UV attenuation by the caged compound in the solution. For the particular conditions (caged compound type and concentration, fluid levels) used here, we estimate UV attenuation to account for <2% of the response variability.

Electrophysiology. Pyramidal neurons 40–100 μm below the surface of the slice were visualized with differential interference contrast (DIC) optics. In addition to identifying these cells as pyramidal neurons based on their DIC appearance, we routinely confirmed that their spike properties, as assayed before mapping by depolarizing current injections, and dendritic arbor morphologies, as assayed after mapping by epifluorescence imaging, were as expected for L2/3 pyramidal neurons (Petersen and Sakmann, 2001; Lübke et al., 2003; Maravall et al., 2004). Cells were patched with borosilicate electrodes and recorded at room temperature in whole-cell mode. Data were acquired with an Axopatch 200B or Multiclamp 700 amplifier (Molecular Devices, Union City, CA), data acquisition boards (models PCI MIO 16E-4 and 6713; National Instruments, Austin, TX), and custom Matlab (Mathworks, Natick, MA) routines. Responses were filtered at 5 kHz and digitized at 10 kHz. The intracellular solution consisted of the following (in mM): 120 $KMeSO_3$, 20 KCl, 4 NaCl, 10 HEPES, 1 EGTA, 4 Mg_2ATP, 0.3 Na_2GTP, 14 Na-phosphocreatine, 3 ascorbate, and 0.05 Alexa-594 hydrazide (Molecular Probes, Eugene, OR), pH 7.25. Currents were measured at a holding potential of −65 mV.

Video imaging. At low magnification (4× objective lens, 0.16 NA; UPlanApo; Olympus), the major columnar (barrels and septa) and laminar (particularly layers 2/3, 4, 5A, and 5B) landmarks of the barrel field in slices were visualized under (bright-field) transillumination (see Fig. 1*aiv*) (Agmon and Connors, 1991; Petersen and Sakmann, 2000). These cytoarchitectonic features were used to align the slice for LSPS mapping (see below) and to define regions of interest for analysis. To establish patch recording, neurons were visualized at high magnification (60× objective, 0.9 NA; LUMPlanFl/IR; Olympus) with video-enhanced infrared-DIC optics. The CCD signal was fed to an analog camera controller (C2741; Hamamatsu, Hamamatsu City, Japan) and from there both to a monitor (for patching) and to a computer, via an A/D converter (DFG/1394-1 FireWire grabber; Imaging Source). The digitized image was used within the LSPS software environment (custom Matlab rou-

tines) to enable precise registration of the uncaging map with the cortical anatomy.

Synaptic input maps. After whole-cell recording was established, the objective lens was switched to 4×, and the stage was moved to align the barrel grid with respect to the stimulus pattern: the 16 × 16 grid of stimulation sites was centered horizontally on either a barrel or a septum and vertically on the L4/L5A boundary (see Fig. 1b,c). Focal photolysis of caged glutamate was accomplished with 1.0 ms flashes from the UV laser. Laser power was nominally set to 15 mW at the specimen plane. The same low-power objective lens was used for visualizing slice landmarks and delivering the UV flash stimuli. The standard map pattern was a 16 × 16 grid with 100 μm spacing (except where noted). The 256 sites within the pattern were visited in a nonraster, nonrandom sequence, following a "shifting-X" pattern designed to avoid revisiting the vicinity of recently stimulated sites (Shepherd et al., 2003). During consecutive mapping, we alternated among eight flipped and rotated variants of this pattern. The interflash interval was 1 s, long enough for responses to subside and to monitor access resistance and whole-cell parameters while permitting maps to be acquired in ~4 min.

Maps of synaptic input were constructed by calculating the mean current amplitude in a response window from 8 to 100 ms after the stimulus. Thus, pixel values represent synaptic charge (coulombs); however, for consistency with previous studies and because synaptic current is a more familiar unit, data are expressed as picoamperes. Responses arriving earlier than the 8 ms window were categorized as direct (i.e., purely postsynaptic) and excluded from additional analysis (Schubert et al., 2001). Two to six maps were obtained per cell, and pixel values were averaged to yield a single mean map per cell. In a subset of analyses, the individual maps were also used as indicated. Maps are presented either as raw pixelated images or as linearly interpolated images (no smoothing applied). Group-average maps were constructed by averaging cells above barrels or septa and in L2 or L3. Because the boundary between L2 and L3 is not cytoarchitectonically distinct, we arbitrarily defined it based on the mean vertical position of the recorded L2/3 cells (546 μm above the L4/L5A border), which was approximately halfway between the top of L2 and the bottom of L3; locating the boundary slightly higher or lower (e.g., ±25 μm) gave essentially identical results. For convenience, we use the terms "L2"and "L3"as shorthand notation for the upper and lower parts of L2/3, respectively.

Excitation profiles. To calibrate the intensity and resolution of photostimulation, we used excitation profiles (Dantzker and Callaway, 2000; Schubert et al., 2001; Shepherd et al., 2003; Brivanlou et al., 2004; Bureau et al., 2004). These single-cell maps of action potentials (APs) stimulated by LSPS provide a measure of the photoexcitability of the types of cells that are the presynaptic partners of the postsynaptic cells recorded during LSPS mapping. Excitation profiles therefore need to be measured for all of the major classes of cells within the mapping field for the LSPS synaptic input maps. Excitation profiles allow one to assess, for example, whether cells differ in photo-excitability from one layer or column to another, or whether cells in a particular region (e.g., in barrels) differ in photo-excitability at different ages (Bureau et al., 2004) or under different sensory deprivation paradigms (Shepherd et al., 2003).

Excitation profiles were measured under almost identical conditions to synaptic input maps, except that neurons were recorded in loose-seal configuration with the amplifier in current-clamp mode, allowing good signal-to-noise recordings of spikes without disrupting the internal state of the cell and potentially perturbing active properties involved in excitability. Control experiments involving dual whole-cell and loose-seal recordings confirmed that the extracellular recording faithfully detected all spikes (data not shown).

To map the spatial distribution of sites of photo-excitability, the objective lens was switched to 4×, and excitation profiles were obtained by mapping over a region large enough to encompass dendritic arbors. In most cases, the map pattern was centered over the cell soma. In two control experiments, the pattern was placed so as to encompass L4 barrel cells while recording from L2/3 neurons, to assess whether photostimulation of barrel cells could cause spiking in L2/3 neurons (i.e., because of synaptic driving by L4 cells). No barrel sites elicited spikes in the L2/3 neurons, even at fourfold higher laser intensity. The standard excitation

profile stimulus pattern was an 8 × 8 shifting-X pattern with 50 or 100 μm spacing; in some experiments, a 16 × 16 grid with 25 μm spacing was used.

Depending on the UV intensity, the location of the uncaging beam relative to the soma and dendrites, and other parameters (see below), photostimulation triggered anywhere from zero to a few spikes. Most spikes occurred with latencies of <15 ms, although latencies of 100–200 ms were observed occasionally, reflecting very slowly rising depolarizations to reach threshold. For the specific experimental conditions used (power level at the objective lens exit pupil ~15 mW; pulse duration, 1 ms; high concentrations of divalent cations in the ACSF), there was reliable perisomatic photostimulation of presynaptic cells while remaining well below the thresholds for photostimulation of distal dendrites or photostimulation through synaptic (network, disynaptic) driving. In particular, based on a data set ($n = 27$ L4 cells; $n = 27$ L5A cells) acquired with a high-density sampling (16 × 16 grid, 25 μm spacing), L4 cells were stimulated to fire 31 ± 6 APs per excitation profile per cell (mean ± SEM), and the resolution, R, calculated as the mean distance from the soma of the spike-generating sites weighted by the number of spikes per site, was 58 ± 3 μm. L5A cells were 1.7-fold more excitable, responding with 53 ± 6 APs per excitation profile per cell, and R was 64 ± 2 μm. In the vicinity of the cell (averaged over an area $R^2\pi$ centered on the excitation profile), the raw excitation profile data correspond for L4 cells to $S_{AP} = 1.84 ± 0.34$ APs per cell per stimulus and for L5A cells to $S_{AP} = 2.59 ± 0.30$ APs per cell per stimulus. Expressing neuronal excitation in this way allows data obtained with different map spacings to be pooled.

We use R, calculated as above, to define "resolution" (Shepherd et al., 2003; Brivanlou et al., 2004). Previously, we found that similar values are obtained by calculating the radii of centroids that capture 50% of the excitation area (Shepherd et al., 2003). For the excitation data in the present study, we found that another metric, the half-width at half-maximum of a Gaussian fitted to plots of the number of APs as a function of the distance from the soma, also gave statistically indistinguishable results (L4, 56 ± 4 μm; L5A, 65 ± 3 μm). In addition to estimating R, the effective radius of photostimulation, it is useful to estimate the volume of neuropil containing the excited neurons ["excitation volume" (V_{exc})]. Approximating V_{exc} as the volume of a sphere of radius R gives values of $8.2 × 10^5$ μm^3 for L4 and $1.5 × 10^6$ μm^3 for L5A.

Morphological reconstructions. Dendritic arbors of L2/3, L4, and L5A cells were reconstructed using Neurolucida (MicroBrightField, Williston, VT). Dendritic length density (Uttley, 1955; Brecht and Sakmann, 2002; Bureau et al., 2004; Shepherd et al., 2005) was calculated per 25 μm pixel and interpolated for display.

Statistical analysis. Unless specified otherwise, data are presented as mean ± SEM, t tests were used for statistical comparisons, and significance was defined as $p < 0.05$.

Results

Functional projections to individual L2/3 pyramidal neurons

We prepared slices of the barrel cortex from young adult rats and recorded functional input maps (spatial maps of excitatory synaptic input) for individual L2/3 pyramidal neurons using LSPS (Fig. 1). Barrels and septa were identified with transillumination in bright-field microscopy (Petersen and Sakmann, 2000). We recorded from L2/3 pyramidal neurons above barrels and septa (Fig. 1a,b) while exciting clusters of neurons by photorelease of glutamate in the focal spot of a UV laser beam on a 16 × 16 pixel grid (Fig. 1c,d). The amplitudes of postsynaptic responses indicate the strength of input to the recorded neuron from the region of the brain slice excited by glutamate uncaging. EPSCs were isolated by voltage-clamping neurons at the inhibitory reversal potential, where amplitudes of IPSCs are negligibly small. Reversal potentials for synaptic inputs to L2/3 neurons from L4 and L5 were 0–10 mV (Shepherd et al., 2003) (our unpublished observations), indicating that these translaminar projections were predominantly excitatory.

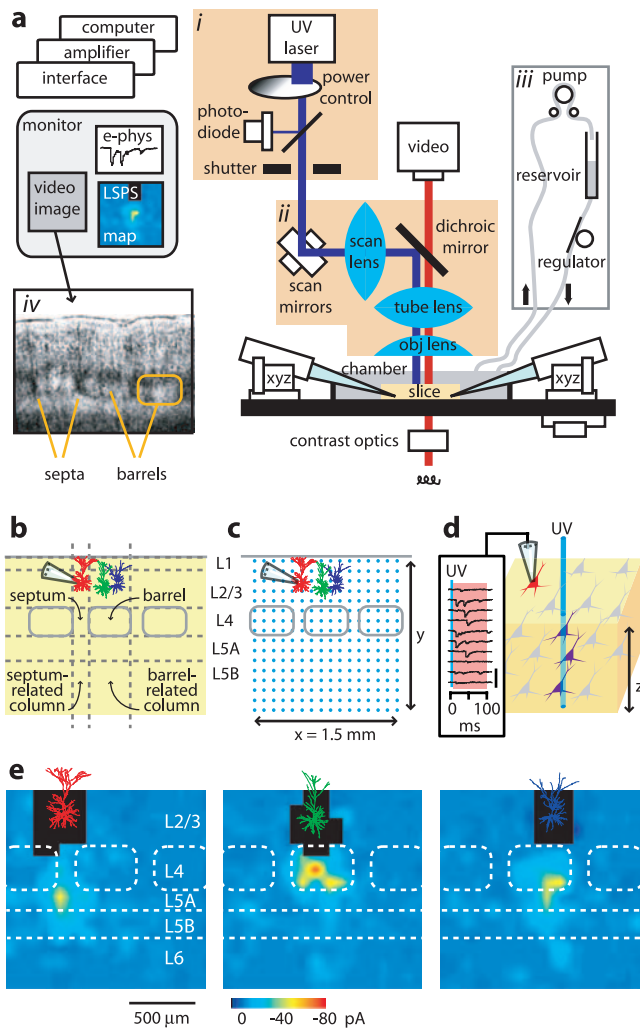LSPS measures the functional strength of excitatory synaptic

Figure 1. Mapping inputs to L2/3 neurons with LSPS. ***a***, Layout of the LSPS microscope. The UV laser and components involved in controlling the timing and power of the beam are shown in ***i***. The scanning system (***ii***) provides spatial control. The recirculating perfusion system is shown in ***iii***. The video image is shown in ***iv***. e-phys, Electrophysiological. ***b***, Barrels and septa in L4 demarcate cortical columns. One septum-related (red) and two barrel-related L2/3 pyramidal cells in the same slice were morphologically reconstructed after functional mapping by LSPS. ***c***, Blue dots (100 µm spacing) mark the LSPS mapping pattern. ***d***, During mapping, each UV flash stimulates APs in a small cluster of neurons (purple), some of which project synaptically to the postsynaptic neuron (red). Inset, Typical traces obtained during photostimulation mapping; the blue line indicates the timing of the UV flash, and the light red region just to the right of this is the window over which responses are averaged. Vertical calibration bar, 50 pA. ***e***, Single-cell examples of LSPS maps of excitatory synaptic input to an L2/3 neuron in particular locations with respect to the L4 barrel/septum grid. For the septum-related neuron (left), the predominant source of excitatory input was from L5A. For the barrel-related neurons (middle and right), L4 provided most of the input, with a smaller contribution from L5A.

projections, not unitary connection strengths. At a particular spot (i.e., pixel) on the grid (Fig. 1*d*), the amplitude of the postsynaptic response is proportional to the number of neurons stimulated, N_{cell} (equal to the product of the neuronal density, ρ_{cell}, and the volume of excited neurons, V_{exc}), the number of APs fired per stimulated neuron (S_{AP}), and the average strength of the synaptic connection with the stimulated presynaptic neuron (q_{con}) (Bureau et al., 2004):

$$\text{Pixel value} \propto \rho_{cell}\, V_{exc}\, S_{AP}\, q_{con}. \qquad (1)$$

Inspection of input maps (Fig. 1*e*) indicated that L2/3 cells received input from layers 2/3, 4, and 5A, primarily in the home

column, with only weak inputs from layers 5B and 6. Individual neurons exhibited distinct spatial patterns of inputs depending on their particular location with respect to the columnar boundaries defined by barrels and septa in L4. Barrel-related L2/3 (L2/3 [barrel]) neurons (Fig. 1, middle and right) received strongest inputs from L4 barrels, often with additional inputs from L5A. This laminar pattern is consistent with functional input maps both from the barrel cortex of younger rats (Shepherd et al., 2003; Bureau et al., 2004) and the rat visual cortex (Dantzker and Callaway, 2000). In contrast, septum-related L2/3 (L2/3 [septum]) neurons (Fig. 1*e*, left) received not only weaker L4 inputs (Shepherd et al., 2003) but also, surprisingly, a strong focus of input from L5A. This was unanticipated, because (1) L4 is generally considered to be the driving source of excitatory input to L2/3 neurons in the sensory cortex (Callaway, 1998; Douglas and Martin, 2004), (2) functional L5→2/3 connectivity was weak in the rat barrel cortex at P14–16 (Shepherd et al., 2003; Bureau et al., 2004), and (3) functional L5→2/3 connectivity has not been detected in pair recordings (Reyes and Sakmann, 1999; Thomson et al., 2002). Strong direct excitation of postsynaptic dendrites by glutamate uncaging (Fig. 1*e*, black pixels) made the quantification of local L2/3→2/3 projections difficult.

Control experiments using excitation profiles established that LSPS maps represent sources of monosynaptic input with sublaminar and sub-columnar resolution (~60 µm) (Fig. 2) (see Materials and Methods). In these experiments, neurons of interest (i.e., located in regions providing synaptic input in LSPS maps) are recorded in loose-seal mode to detect APs (Fig. 2*a*). This allows the locations of AP generating sites, relative to the soma, to be mapped (Fig. 2*b*). As seen in the average excitation profiles of L4 and L5A neurons (Fig. 2*c*), spikes tend to occur only if the uncaging beam is very close to the soma. The spatial resolution, R, for exciting neurons was essentially independent of cell depth and laser power (Fig. 2*e*). In contrast, neuronal excitation, S_{AP} (number of APs evoked per cell by photostimulation), fell exponentially with soma depth and grew linearly with laser power (Fig. 2*f*).

Responses from L5A clearly originated from L5A neurons, and not from activation of dangling dendrites of L4 cells. Because the dendrites of L4 cells are strongly polarized toward barrel centers (Petersen and Sakmann, 2000), their density in L5A is extremely low. Excitation profiles (see Methods) showed that photoexcitation of cells occurred only close to the soma and thus within L4 (Fig. 2). In separate control experiments, we recorded excitation profiles from L4 cells located within ~50 µm of the L4/5A border (n = 6 cells), and never observed excitation of L4 cells using stimuli in L5A corresponding to those used to map inputs here. Moreover, in LSPS maps, sites of L5A input frequently occurred separate from sites of L4 inputs, and L5A inputs even exceeded L4 inputs to L2 [septum] cells (Fig. 1*e*, left).

Average projections to L2 and L3 cells above barrels and septa
We recorded from L2/3 pyramidal cells (n = 32 cells, 15 slices, 10 animals) in four positionally defined populations, as defined by laminar (L2 vs L3) and columnar (barrel vs septum related) location, and averaged the input maps within each group (Fig. 3) (see Materials and Methods). Because the boundary between L2 and L3 is poorly defined, we use the terms L2 and L3 to refer to the upper and lower regions of L2/3, respectively (see Materials and Methods). In barrel-related columns, cells in both L2 (Fig. 3*a*) and L3 (Fig. 3*b*) exhibited strong L4 barrel inputs and weaker L5A inputs (Fig. 3*a*,*b*,*e*). In septum-related columns, L2 cells (Fig. 3*c*) received significantly stronger L5A inputs than L3 cells (Fig. 3*d*)
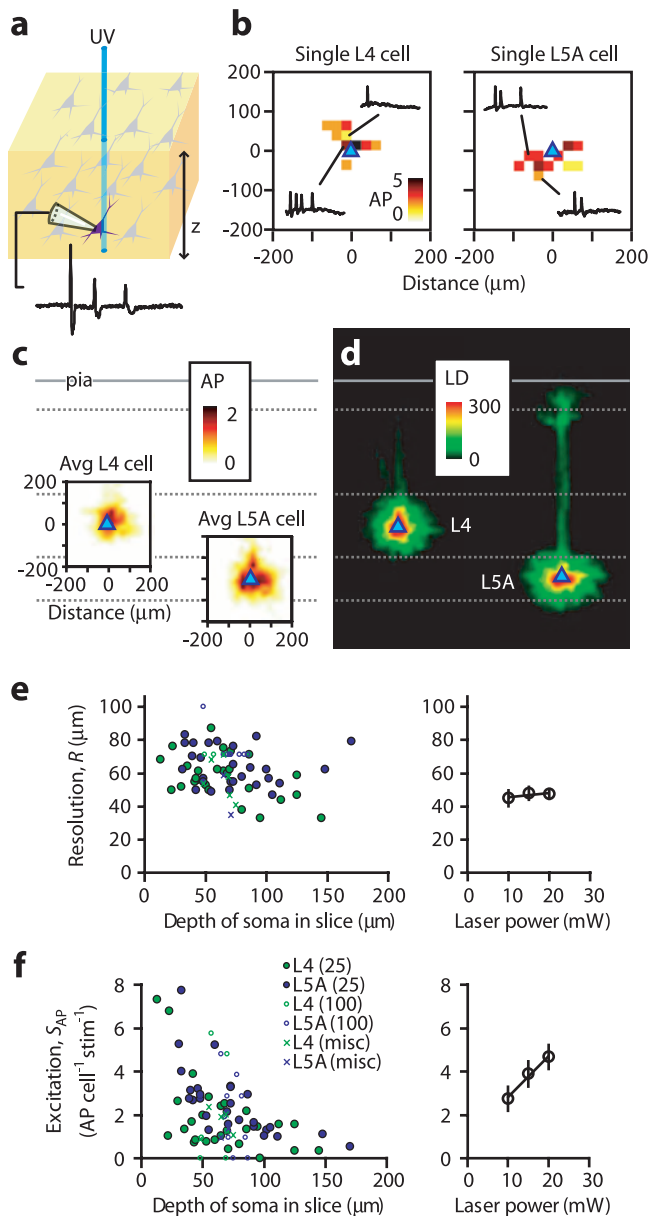
Figure 2. Calibration of LSPS using excitation profiles. **a**, Schematic of the excitation profile recording arrangement. A neuron in a presynaptic layer of the slice is recorded in loose-seal mode to detect APs generated by UV stimuli. **b**, Single-cell examples of excitation profiles of L4 cells (left) and L5A cells (right). Maps (25 μm spacing) were soma centered (triangles). **c**, Average excitation profiles of L4 and L5A cells, plotted on an approximate scale of cortical laminas. Avg, Average. **d**, Plots of dendritic length density (see Materials and Methods) are shown for comparison; same scale as in **c**. **e**, Resolution as a function of soma depth (left) and laser power (right). The legend in **f** shows cell types and spacing used for mapping; the "misc" group includes maps from experiments with varying grid parameters (64 or 256 sites; 20, 25, or 100 μm spacing). **f**, Neuronal excitation as a function of soma depth (left) and laser power (right). See Materials and Methods for definitions and methods relating to resolution and excitation parameters.

despite being more distant targets; L4 inputs were weak (Shepherd et al., 2003; Bureau et al., 2004) (Fig. 3c–e). The L5A→2 septum projection was as strong as the L4→2/3 barrel projections (Fig. 3e). In the average map (Fig. 3c), the strong focus of L5A input exhibited a small offset, extending from directly below the septum anteromedially (toward the right in the map) under the neighboring barrel. Projection strengths did not differ significantly among the three strongest L4/5A→2/3 projections (i.e.,

L4→2 barrel, L4→3 barrel, and L5A→2 septum) or among the five weaker L4/5A→2/3 projections (i.e., L4→2 septum, L4→3 septum, L5A→2 barrel, L5A→3 barrel, and L5A→3 septum), but each of the strongest projections differed significantly from the weaker ones, by a factor of ~2 (Fig. 3e).

Inputs from L5B were weaker than inputs from L4 and 5A (Fig. 3e). Unlike the L4- and L5A-originating projections, projection strengths did not differ significantly among the four different L5B-originating projections. Inputs from L5B, although weak, were all significantly stronger than inputs from L6, which were close to zero (Fig. 3e).

To calculate the input strength per presynaptic neuron per AP (q_{con}), we divided the maps by the excitation parameters $\rho_{cell} V_{exc} S_{AP}$ (Eq. 1). ρ_{cell} is 2.1-fold greater in L4 than in L5A (Ren et al., 1992; Keller and Carlson, 1999), and, on average, S_{AP} was 1.4-fold greater and V_{exc} was 1.8-fold greater in L5A than in L4 (see Materials and Methods). Because the overall difference in the L4 and L5A excitation parameters were small (e.g., the ratio of $\rho_{cell} V_{exc} S_{AP}$ for L4 vs L5A was 1.12), the relative differences in strength of L4- and L5A-originating projections were essentially unchanged (Fig. 3f). For example, q_{con} for L5A→2 septum was comparable with that of the L4→2/3 barrel projections. The ratio of q_{con} for L5A to q_{con} for L4 was low (~0.5) for barrel-related projections to L2 and L3, high (~2.4) for septum-related projections to L2, and closer to 1 for septum-related projections to L3.

From these input map measurements of functional excitatory projections to positionally defined populations of L2/3 neurons, we draw the following conclusions (Fig. 3e,f). In barrel-related columns, excitatory synaptic input arrives primarily via the L4→2/3 projection, with a substantial but significantly lower contribution of L5A input. Furthermore, there is little differentiation at the circuit level between L2 and L3 pyramids. In septum-related columns, the functional organization is strikingly different, with L5A→2 septum providing the dominant source of input.

Correlation analysis of individual maps

To explore in greater depth the spatial organization of these circuits, we combined LSPS with simultaneous or sequential recording of multiple neurons in the same slice. In these experiments, we used both young adult and juvenile animals, allowing us to test for age-dependent differences in the strengths of both synaptic inputs and map-to-map correlations. We kept track of both the intersomatic distance between the neurons and the locations of the cells with respect to the columnar topography (i.e., whether neurons were in barrel- or septum-related columns). Examples of two simultaneously mapped pairs (Fig. 4a,b) demonstrate basic features of these maps (shown as raw images to emphasize individual pixel values).

First, pixel-to-pixel variability within individual maps was high, giving a granular appearance to the maps. That is, "hot spots" supplying over 100 pA of synaptic input current lay adjacent to "cold spots" with little or no detectable current (Fig. 4c; supplementary Fig. S1, available at www.jneurosci.org as supplemental material). This was not attributable to trial-to-trial variations, because maps were consistent across multiple repetitions (see below) (supplementary Fig. S1, available at www.jneurosci.org as supplemental material) (Shepherd et al., 2003). Second, as seen in the average maps (see above), the input map topography of L2/3 pyramidal neurons seemed to follow column-specific patterns: cells above barrels (Fig. 4a) received strongest inputs from L4 barrels immediately below them, with additional home-column input from L5A, whereas cells
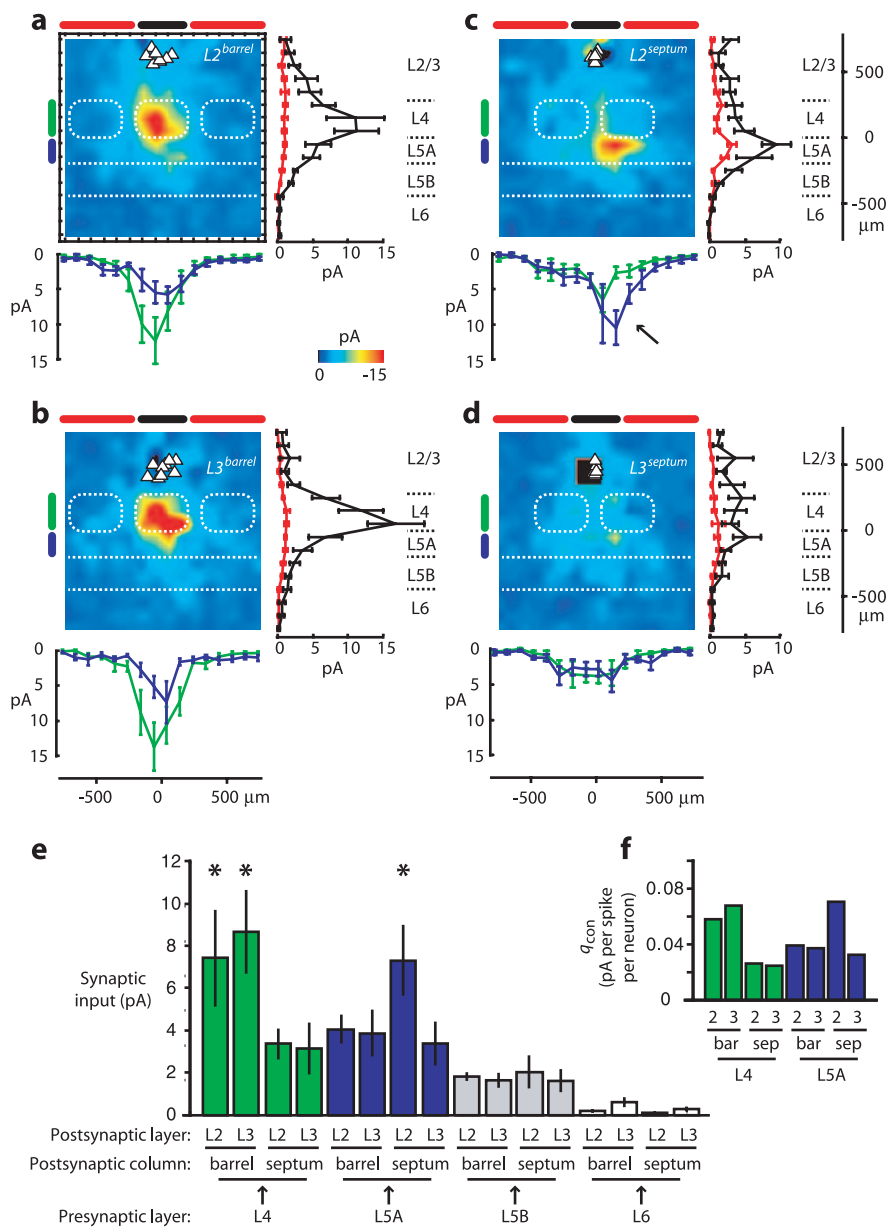
Figure 3. Average input maps for L2/3 pyramidal cells grouped by columnar and laminar location. ***a***, L2 ^{barrel} cells ($n = 8$). The plot below the map shows horizontal profiles (100 μm bins, mean $\pm$ SEM) of input from L4 (green line; data from region indicated by the vertical green bar to the left of the map) and L5A (blue line). Barrels and laminar boundaries are drawn as dashed lines. Plots to the right of maps show vertical profiles of home-column input (black line; data from region indicated by the horizontal black bar above the map) and (average) side-column input (red line). ***b***, L3 ^{barrel} cells ($n = 9$). ***c***, L2 ^{septum} cells ($n = 8$). The arrow in the plot points to the focus of strong input from L5A. ***d***, L3 ^{septum} cells ($n = 7$). ***e***, Average synaptic input for excitatory synaptic projections defined by the presynaptic layer, postsynaptic layer, and postsynaptic column. The three strongest L4/5A→2/3 projections (asterisks) were significantly stronger compared with all other projections. The five weaker L4/5A→2/3 projections were significantly stronger compared with L5B- and L6-originating projections, with the exception of L4→3 ^{septum} versus L5B→2 ^{septum}. The four L5B-based projections were all significantly stronger than the four L6-based projections. ***f***, Average q_{con} for the projections originating from L4 and L5A. bar, Barrel; sep, septum.

caging at many sites, in particular the hot spots, produced complex postsynaptic currents without refractory periods (Fig. 4c, arrow), indicating that several connected neurons were excited. Uncaging at other sites resulted in simple postsynaptic current waveforms (Fig. 4c, asterisk), consistent with the possibility that just one or two presynaptic neurons were involved (see also supplementary Fig. S1, available at www.jneurosci.org as supplemental material).

To quantify similarities and differences in input maps for pairs of neurons, we computed correlation coefficients on a pixel-by-pixel basis. That is, each pixel value from one cell is compared with the corresponding pixel value from the neighboring cell (Fig. 4a,b, right). In the example in which both cells were above the same barrel (Fig. 4a), the correlation coefficient was high (0.83), reflecting the fact that the maps were similar and shared identical hot spots. In contrast, in the example of two septum-related cells (Fig. 4b), the maps also appeared generally similar; however, the correlation coefficient was low (0.35) because the maps differed substantially in local detail.

To make multiple pairwise correlations, we needed to map multiple neurons per slice. An analysis of simultaneously mapped cells indicated that maps recorded simultaneously or non-simultaneously (i.e., sequentially in the same slice, using identical stimulation grid coordinates) were statistically indistinguishable (supplementary Fig. S2, available at www.jneurosci.org as supplemental material). We therefore used a combination of simultaneous and sequential mapping to record input maps for groups of two to four neurons per slice in 21 slices ($n = 17$ animals). For each cell, we calculated a single average map from the two to six individual mapping trials, and for each group of two to four neurons from the same slice, we performed all possible pairwise comparisons and computed correlation coefficients (i.e., one to six comparisons per group).

First, we tested whether developmental age influenced the strength or spatial distribution of inputs. Mean synaptic input in the maps increased significantly by a factor of 1.6 with development from juvenile (mean input, 1.09 $\pm$ 0.10 pA; average of all pixels $\pm$ SEM; age, P13–P19; $n = 29$ cells) to adult (mean input, 1.72 $\pm$ 0.20 pA; age, P25–P36; $n = 18$ cells). In contrast, correlation coefficients did not vary significantly between juveniles (mean, $r = 0.46 \pm 0.06$; $n = 16$ pairwise comparisons) and adults (mean, $r = 0.42 \pm 0.06$; $n = 16$ pairwise comparisons).

We next evaluated how correlations depend on the intersomatic distance between neurons, as a measure of the length scale of circuit correlation (Fig. 4d). The distance dependence of cir-

above septa (Fig. 4b) received inputs from a wider horizontal expanse in L5A, plus occasional hot spots in L4. Maps from pairs of barrel-related neurons in the same column (Fig. 4c; supplementary Fig. S1, available at www.jneurosci.org as supplemental material) were similar.

Inspection of the traces from consecutive maps recorded simultaneously from pairs of neurons also reveals the nature of the spatial graininess of the maps (Fig. 4c; supplementary Fig. S1, available at www.jneurosci.org as supplemental material). Un-

cuit correlation differed according to the columnar location of the two neurons constituting a pair. In particular, when both neurons were barrel-related cells, the correlation was consistently high ($r = 0.64 \pm 0.03$; range, 0.41–0.83; $n = 15$ comparisons) and sustained over the full extent of the barrel (i.e., correlations were relatively independent of precise location within the barrel column). In contrast, when one or more cells in the pair were not in the home barrel-related column, the correlation was lower, and the drop-off with intersomatic separation was steep. Fitting an exponential to the barrel/barrel data yielded a length constant, λ, of 2.13 mm [95% confidence interval (CI), −3.30, 7.55], whereas fitting an exponential to the other data (excluding three data points >300 μm, to fit over a comparable range of distances) yielded a significantly shorter λ of 0.20 mm (95% CI, 1.41, 2.61). Thus, circuit correlation was a discontinuous function of distance for barrel-related cells, in that it critically depended on the columnar identity of the other cell in the pair. Septum-related cells, in contrast, showed a continuous, monotonically declining dependence on distance for their circuit correlation.

From the neighboring-neuron analyses, we draw the following conclusions. First, the pair-mapping approach demonstrates quantitatively that L2/3 barrel- and septum-related neurons belong to distinct columnar systems, confirming at the single-cell level similar conclusions reached by averaging across multiple cells. Additionally, correlation analysis revealed an aspect of circuit organization that was lost in the averaging approach: L2/3 neurons were more likely to share detailed features of input circuits when both cells were colocalized to the same barrel-related column than if at least one of the cells was not, suggesting additional fundamental differences in circuit organization in the two columnar systems than indicated by the averaging approach alone.

Figure 4. Neighboring-neuron mapping. *a*, Average LSPS maps of simultaneously recorded synaptic inputs to a pair of neighboring L2/3 [barrel] neurons. The intersomatic distance was ~100 μm. Schematics shows cell positions with respect to barrels. Both cells received strong barrel inputs and also L5A inputs. Electrophysiological traces for pixels within the dashed yellow boxes are shown in *c* and supplementary Figure S1 (available at www.jneurosci.org as supplemental material). The plot shows the pixel-wise comparison of the 256 pixel values of cell a versus the corresponding values for cell b. For this pair, approximately six sites gave strong input to both cells, as reflected in the high correlation coefficient (*r*). Some sites gave inputs only to one of the cells, yielding points that fall along the zero lines (horizontal/vertical dashed lines). The diagonal dashed line (slope = 1) represents perfect correlation. *b*, A pair of cells close together (~25 μm) in the same septum-related column. The maps are globally similar but differ substantially in local detail, as reflected in the lower correlation coefficient. Inputs were predominantly from L5 and L2/3, with some L4 inputs as well. *c*, Traces from an individual map trial corresponding to the 48 pixels in the boxed region (dashed yellow rectangles) of the maps in *a*. Calibration: 100 pA, 100 ms. Asterisk, Simple postsynaptic current waveform; arrow, complex postsynaptic current waveform. *d*, Spatial length scales of correlation. Correlation coefficients, *r*, as a function of intersomatic distance, for different neighboring-neuron pair combinations of L2/3 pyramidal neurons in barrel-related (B) and septum-related (S) columns, as indicated in the legend. Same-barrel B/B pairs (black symbols) are distinguished from all other types of pairs (red symbols). Exponential curves were fit to the overlapping (common) region along the x-axis of the two data sets (e.g., 3 data points in the "all other" set were excluded), and the curves are extended as dashed lines beyond the region of overlap.

Discussion

We used quantitative LSPS to map the spatial distribution of functional excitatory synaptic input to individual L2/3 pyramidal neurons in the rat's barrel cortex, finding that the functional organization of projections to L2/3 neurons depends on their specific locations relative to barrels and septa.

Parallel interdigitating pathways in the barrel cortex

By mapping synaptic inputs originating from two laminas (L4 and L5A) and terminating onto pyramidal neurons located in two laminas (L2 and L3) and two columns (barrel and septum related), we functionally characterized eight positionally defined intracortical projections in the rat's barrel cortex (Fig. 5). Inputs to neurons in ba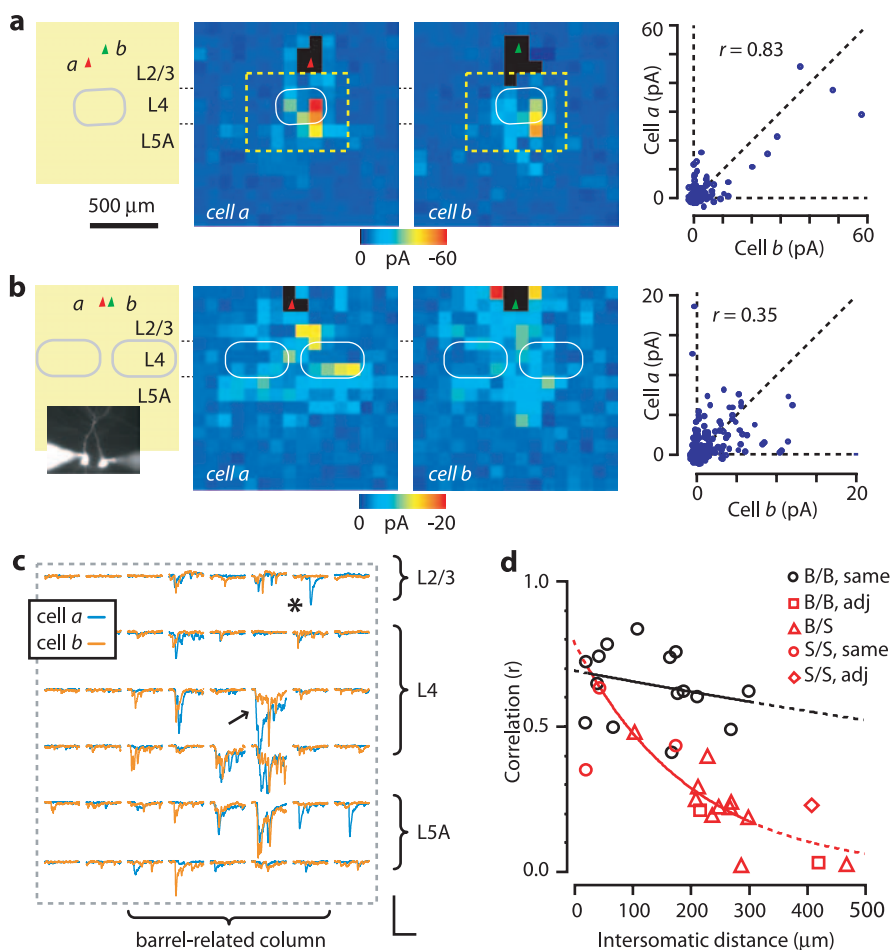rrel-related columns were dominated by the L4→2/3 projections, consistent with previous results (Shepherd et al., 2003; Bureau et al., 2004) and with the idea that, in the sensory neocortex, thalamic signals arrive in L4 and ascend via L4→2/3 projections (Petersen and Sakmann, 2001; Douglas and Martin, 2004). The strong focus of excitatory input from L5A to L2 [septum] was unanticipated, both because L5→2 connectivity has been notably scarce in *in vitro* pair recordings (Reyes and Sakmann, 1999; Thomson et al., 2002) and because the major source of excitatory intracortical input to supragranular layers in the sensory neocortex is generally thought to be L4 (Callaway, 1998; Dantzker and Callaway, 2000; Douglas and Martin, 2004). However, the subcortical organization of the vibrissa system into lemniscal [via the ventral posterior medial (VPM) nucleus in the

thalamus] and paralemniscal [via the medial division of the posterior nucleus (POm) in the thalamus] channels (Armstrong-James, 1995; Ahissar et al., 2000) suggests an important role for this projection. Based on receptive-field properties of barrel cortical neurons, lemniscal and paralemniscal pathways appear to segregate by column in L2–L4 (lemniscal→barrel related; paralemniscal→septum related) but by layer in L5 (lemniscal→L5B; paralemniscal→L5A) (Ahissar et al., 2000; Brecht and Sakmann, 2002; Brecht et al., 2003; Manns et al., 2004). Lemniscal→L4 and paralemniscal→L5A projections have also been identified anatomically, based on anterograde tracer injections into the VPM and POm (Koralek et al., 1988; Chmielowska et al., 1989; Lu and Lin, 1992). We speculate that this L5A→2 ^{septum} projection represents an intracortical continuation of the paralemniscal pathway, providing a mechanism for the transfer of paralemniscal excitation to supragranular layers (Fig. 5).

The L5A→2 ^{septum} projection displayed, on average, a small anteromedial offset (Fig. 3c), implying that L5A neurons in this region project to the posterolateral septum-related column. This offset was evident in many but not all of the maps of the individual neurons (compare Fig. 1e, left) and did not appear to correlate with any particular septum in the barrel field (i.e., septum "A/B" vs "B/C," etc.). A similar but weaker offset was observed for the average L5A→2 ^{barrel} (Fig. 3a) and L5A→3 ^{barrel} (Fig. 3b) projections, whereas the average L4→L2/3 ^{barrel} projections showed a subtle shift in the opposite direction. We speculate that these small horizontal offsets in translaminar projections could mediate short-range lateral propagation of excitatory signals such as have been proposed on the basis of response latencies (for review, Armstrong-James, 1995).

Interestingly, although average strength of synaptic inputs to L2/3 pyramidal neurons increased significantly from juvenile to young adult animals, correlation coefficients, which reflect the spatial distribution of synaptic input, did not. One interpretation of this is that while physiological maturation of synapses in these projections continues to mature over this time scale, the spatial organization (e.g., laminar and columnar topography) is relatively stable at this stage of development. This is consistent with observations of functional (Bureau et al., 2004) and structural (Bender et al., 2003; Bureau et al., 2004) features of cortical columnar organization at earlier developmental stages.

Local circuits of neighboring neurons

Using LSPS, we mapped the excitatory synaptic inputs to neighboring L2/3 neurons and analyzed these in terms of the locations of the cells within the barrel- and septum-related columnar organization of the barrel cortex. Our main findings from the neighboring-neuron analysis are as follows. Circuit organization in barrel-related columns was strikingly different from that in septum-related columns (Fig. 5). Within the same barrel-related column, pairwise comparisons of L2/3 ^{barrel} neurons showed similar input patterns. This circuit-sharing was mainly independent of the intersomatic distance between neurons: neurons on "opposite sides" of a barrel-related column still had highly correlated input maps. The pairwise comparisons (Fig. 4d) together with the average maps (Fig. 3a,b) of L2/3 ^{barrel} neurons thus indicate that the functional organization of local excitatory inputs for these cells is essentially determined at the level of columnar identity and not on their particular locations within the L2/3 ^{barrel} region. In contrast, when neurons did not share the same barrel-related column (e.g., L2/3 ^{septum}–L2/3 ^{septum} pairs, L2/3 ^{septum}–L2/3 ^{barrel} pairs), correlations between input maps depended steeply on the
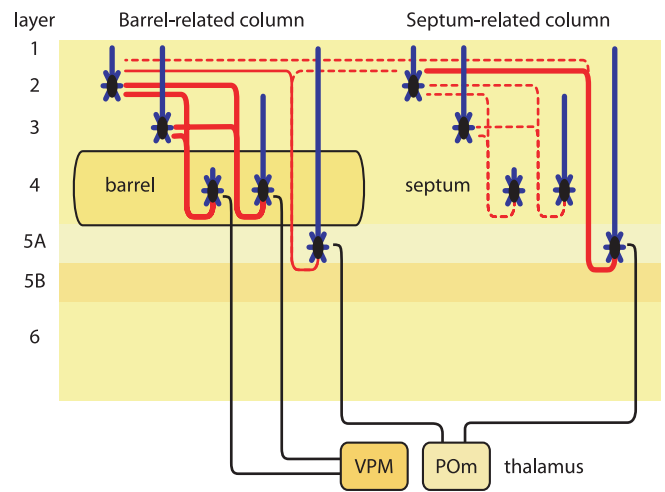

Figure 5. "Wiring diagram" of excitatory synaptic projections from barrel- and septum-related cells in L4 and L5A to L2/3 pyramidal neurons in the barrel cortex. Thick red lines represent the strongest projections, thin lines represent the moderately strong projections, and dashed lines represent the variable and/or weak projections. Thalamic projections to L4 and 5A are drawn as solid black lines. VPM→barrel→L2/3 ^{barrel} and POm→L5A→L2 ^{septum} are organized as parallel interdigitating pathways.

intersomatic distance separating the cells. These pairwise comparisons (Fig. 4d) thus also corroborate the average maps (Fig. 3c,d), which showed different input patterns for L2 ^{septum} versus L3 ^{septum} neurons. Although we previously have shown differences in input organization based on average maps obtained by pooling neurons from multiple slices and animals (Shepherd et al., 2003), here we demonstrate that these local-circuit differences are detectable at the level of individual neighboring neurons.

LSPS is a powerful tool for neocortical circuit analysis for multiple reasons, among them the fact that resolution is high (because stimulation occurs close to the soma of cells, and not at axons or distal dendrites) and mapping (of hundreds of sites) is rapid. Previously, we characterized the within-cell variability in input maps, demonstrating that it is low (i.e., maps are highly reproducible) (Shepherd et al., 2003). Here, in addition to extending this observation using correlation analysis ($r = \sim 0.75$ for same-cell map comparisons) (supplementary Fig. S2, available at www.jneurosci.org as supplemental material), we characterized the between-cell variability by comparing maps from multiple cells recorded in the same or different slices (supplementary Fig. S2, available at www.jneurosci.org as supplemental material). As gauged by correlation analysis, input patterns of neighboring neurons were highly similar when both cells were in the same barrel-related column, independent of the intersomatic distance; if they were not, correlations fell sharply with intersomatic distance toward chance levels (Fig. 4d). Circuits therefore change discontinuously across barrel–septum boundaries, providing quantitative support for interdigitating barrel- and septum-related columns (Fig. 5).

It is interesting to compare our results with those obtained using other approaches for studying circuits of neighboring neurons. Most have used *in vivo* physiological recording of spike patterns, either using the approach of comparing sequential single-unit recordings or simultaneous multiunit recordings. As discussed by Jung et al. (2000), the classical view (Mountcastle, 1957; Hubel and Wiesel, 1962; Rao et al., 1999) holds that the cortical column is the basic computational unit, with (vertically) neighboring neurons in the same column processing similar information. A number of studies have obtained results consistent

with this, finding significantly high mean correlation coefficients for neighboring neurons in monkey MT (Zohary et al., 1994) and the perirhinal cortex (Erickson et al., 2000) and cat V1 (van Kan et al., 1985; DeAngelis et al., 1999). An alternative view is that response patterns vary widely within the column (Jung et al., 2000, and references therein). Recent work (Reich et al., 2001) has shown both independence and redundancy in small local groups of monkey V1 neurons recorded with tetrodes; signal correlations generally did not exceed 0.25, however. Similarly, in the rat hippocampus, evidence has been presented in favor both of clustering (Eichenbaum et al., 1989; Hampson et al., 1999) and of independence (Redish et al., 2001) of firing parameters.

The classical model would predict that synaptic circuits are shared among neighboring neurons, whereas the alternative model would predict that they are not. In the present study, we found evidence in favor of both models: we found high correlations between the local circuits of neighboring L2/3 [barrel] pyramidal neurons sharing the same barrel-related column and low correlations between cells that did not share the same barrel-related column and that were separated by an intersomatic distance of $\sim 50\ \mu m$ or greater. Thus, in the barrel cortex, input circuits are strongly location dependent. An interesting issue for future studies is the extent to which neighboring neurons in other cortical regions, including sensory, motor, and association areas, share input circuits.

References

Agmon A, Connors BW (1991) Thalamocortical responses of mouse somatosensory (barrel) cortex in vitro. Neuroscience 41:365–379.

Ahissar E, Sosnik R, Haidarliu S (2000) Transformation from temporal to rate coding in a somatosensory thalamocortical pathway. Nature 406:302–306.

Allen CB, Celikel T, Feldman DE (2003) Long-term depression induced by sensory deprivation during cortical map plasticity in vivo. Nat Neurosci 6:291–299.

Armstrong-James M (1995) The nature and plasticity of sensory processing within adut rat barrel cortex. In: The barrel cortex of rodents, Ed 1 (Jones EG, Diamond IT, eds), p 446. New York: Plenum.

Armstrong-James M, Fox K (1987) Spatiotemporal convergence and divergence in the rat S1 "barrel" cortex. J Comp Neurol 263:265–281.

Armstrong-James M, Fox K, Das-Gupta A (1992) Flow of excitation within rat barrel cortex on striking a single vibrissa. J Neurosci 68:1345–1354.

Bender KJ, Rangel J, Feldman DE (2003) Development of columnar topography in the excitatory layer 4 to layer 2/3 projection in rat barrel cortex. J Neurosci 23:8759–8770.

Brecht M, Sakmann B (2002) Dynamic representation of whisker deflection by synaptic potentials in spiny stellate and pyramidal cells in the barrels and septa of layer 4 rat somatosensory cortex. J Physiol (Lond) 543:49–70.

Brecht M, Roth A, Sakmann B (2003) Dynamic receptive fields of reconstructed pyramidal cells in layers 3 and 2 of rat somatosensory barrel cortex. J Physiol (Lond) 553:243–265.

Brivanlou IH, Dantzker JL, Stevens CF, Callaway EM (2004) Topographic specificity of functional connections from hippocampal CA3 to CA1. Proc Natl Acad Sci USA 101:2560–2565.

Bureau I, Shepherd GMG, Svoboda K (2004) Precise development of functional and anatomical columns in the neocortex. Neuron 42:789–801.

Callaway EM (1998) Local circuits in primary visual cortex of the macaque monkey. Annu Rev Neurosci 21:47–74.

Callaway EM, Katz LC (1993) Photostimulation using caged glutamate reveals functional circuitry in living brain slices. Proc Natl Acad Sci USA 90:7661–7665.

Canepari M, Nelson L, Papageorgiou G, Corrie JE, Ogden D (2001) Photochemical and pharmacological evaluation of 7-nitroindolinyl- and 4-methoxy-7-nitroindolinyl-amino acids as novel, fast caged neurotransmitters. J Neurosci Methods 112:29–42.

Chmielowska J, Carvell GE, Simons DJ (1989) Spatial organization of thalamocortical and corticothalamic projection systems in the rat SmI barrel cortex. J Comp Neurol 285:325–338.

Dantzker JL, Callaway EM (2000) Laminar sources of synaptic input to cortical inhibitory interneurons and pyramidal neurons. Nat Neurosci 3:701–707.

DeAngelis GC, Ghose GM, Ohzawa I, Freeman RD (1999) Functional micro-organization of primary visual cortex: receptive field analysis of nearby neurons. J Neurosci 19:4046–4064.

Diamond ME, Huang W, Ebner FF (1994) Laminar comparison of somatosensory cortical plasticity. Science 265:1885–1888.

Douglas RJ, Martin KA (2004) Neuronal circuits of the neocortex. Annu Rev Neurosci 27:419–451.

Eichenbaum H, Wiener SI, Shapiro ML, Cohen NJ (1989) The organization of spatial coding in the hippocampus: a study of neural ensemble activity. J Neurosci 9:2764–2775.

Erickson CA, Jagadeesh B, Desimone R (2000) Clustering of perirhinal neurons with similar properties following visual experience in adult monkeys. Nat Neurosci 3:1143–1148.

Feldman DE (2000) Timing-based LTP and LTD at vertical inputs to layer II/III pyramidal cells in rat barrel cortex. Neuron 27:45–56.

Feldmeyer D, Lübke J, Silver RA, Sakmann B (2002) Synaptic connections between layer 4 spiny neurone-layer 2/3 pyramidal cell pairs in juvenile rat barrel cortex: physiology and anatomy of interlaminar signalling within a cortical column. J Physiol (Lond) 538:803–822.

Finnerty GT, Roberts LS, Connors BW (1999) Sensory experience modifies the short-term dynamics of neocortical synapses. Nature 400:367–371.

Foeller E, Feldman DE (2004) Synaptic basis for developmental plasticity in somatosensory cortex. Curr Opin Neurobiol 14:89–95.

Fox K (1992) A critical period for experience-dependent synaptic plasticity in rat barrel cortex. J Neurosci 12:1826–1838.

Fox K (2002) Anatomical pathways and molecular mechanisms for plasticity in the barrel cortex. Neuroscience 111:799–814.

Hampson RE, Simeral JD, Deadwyler SA (1999) Distribution of spatial and nonspatial information in dorsal hippocampus. Nature 402:610–614.

Hubel DH, Wiesel TN (1962) Receptive fields, binocular interaction and functional architecture in the cat's visual cortex. J Physiol (Lond) 148:574–591.

Jung MW, Qin Y, Lee D, Mook-Jung I (2000) Relationship among discharges of neighboring neurons in the rat prefrontal cortex during spatial working memory tasks. J Neurosci 20:6166–6172.

Katz LC, Dalva MB (1994) Scanning laser photostimulation: a new approach for analyzing brain circuits. J Neurosci Methods 54:205–218.

Keller A, Carlson GC (1999) Neonatal whisker clipping alters intracortical, but not thalamocortical projections, in rat barrel cortex. J Comp Neurol 412:83–94.

Kim U, Ebner FF (1999) Barrels and septa: separate circuits in rat barrels field cortex. J Comp Neurol 408:489–505.

Koralek KA, Jensen KF, Killackey HP (1988) Evidence for two complementary patterns of thalamic input to the rat somatosensory cortex. Brain Res 463:346–351.

Lendvai B, Stern E, Chen B, Svoboda K (2000) Experience-dependent plasticity of dendritic spines in the developing rat barrel cortex in vivo. Nature 404:876–881.

Lu SM, Lin RCS (1992) Thalamic afferents of the rat barrel cortex: a light- and electron-microscopic study using Phaseolus vulgaris leucoagglutinin as an anterograde tracer. Somatosens Mot Res 10:1–16.

Lübke J, Roth A, Feldmeyer D, Sakmann B (2003) Morphometric analysis of the columnar innervation domain of neurons connecting layer 4 and layer 2/3 of juvenile rat barrel cortex. Cereb Cortex 13:1051–1063.

Mainen ZF, Maletic-Savatic M, Shi SH, Hayashi Y, Malinow R, Svoboda K (1999) Two-photon imaging in living brain slices. Methods 18:231–239.

Manns ID, Sakmann B, Brecht M (2004) Sub- and suprathreshold receptive field properties of pyramidal neurones in layers 5A and 5B of rat somatosensory barrel cortex. J Physiol (Lond) 556:601–622.

Maravall M, Stern EA, Svoboda K (2004) Development of intrinsic properties and excitability of layer 2/3 pyramidal neurons during a critical period for sensory maps in rat barrel cortex. J Neurophysiol 92:144–156.

Mountcastle VB (1957) Modality and topographic properties of single neurons of cat's somatic sensory cortex. J Neurophysiol 20:408–434.

Petersen CCH, Sakmann B (2000) The excitatory neuronal network of rat layer 4 barrel cortex. J Neurosci 20:7579–7586.

Petersen CCH, Sakmann B (2001) Functionally independent columns of rat somatosensory barrel cortex revealed with voltage-sensitive dye imaging. J Neurosci 21:8435–8446.

Rao SG, Williams GV, Goldman-Rakic PS (1999) Isodirectional tuning of ad-

jacent interneurons and pyramidal cells during working memory: evidence for microcolumnar organization in PFC. J Neurophysiol 81:1903–1916.

Redish AD, Battaglia FP, Chawla MK, Ekstrom AD, Gerrard JL, Lipa P, Rosenzweig ES, Worley PF, Guzowski JF, McNaughton BL, Barnes CA (2001) Independence of firing correlates of anatomically proximate hippocampal pyramidal cells. J Neurosci 21:RC134(1–6).

Reich DS, Mechler F, Victor JD (2001) Independent and redundant information in nearby cortical neurons. Science 294:2566–2568.

Ren JQ, Aika Y, Heizmann CW, Kosaka T (1992) Quantitative analysis of neurons and glial cells in the rat somatosensory cortex, with special reference to GABAergic neurons and parvalbumin-containing neurons. Exp Brain Res 92:1–14.

Reyes A, Sakmann B (1999) Developmental switch in the short-term modification of unitary EPSPs evoked in layer 2/3 and layer 5 pyramidal neurons of rat neocortex. J Neurosci 19:3827–3835.

Rice FL (1995) Comparative aspects of barrel structure and development. In: The barrel cortex of rodents (Jones EG, Diamond IT, eds), pp 1–76. New York: Plenum.

Schubert D, Staiger JF, Cho N, Kötter R, Zilles K, Luhmann HJ (2001) Layer-specific intracolumnar and transcolumnar functional connectivity of layer V pyramidal cells in rat barrel cortex. J Neurosci 21:3580–3592.

Shepherd GMG, Pologruto TA, Svoboda K (2003) Circuit analysis of experience-dependent plasticity in the developing rat barrel cortex. Neuron 38:277–289.

Shepherd GMG, Stepanyants A, Bureau I, Chklovskii D, Svoboda K (2005) Geometric and functional organization of cortical circuits. Nat Neurosci 8:782–790.

Simons DJ (1978) Response properties of vibrissa units in rat SI somatosensory neocortex. J Neurophysiol 41:798–820.

Staiger JF, Flagmeyer I, Schubert D, Zilles K, Kötter R, Luhmann HJ (2004) Functional diversity of layer IV spiny neurons in rat somatosensory cortex: quantitative morphology of electrophysiologically characterized and biocytin labeled cells. Cereb Cortex 14:690–701.

Stern EA, Maravall M, Svoboda K (2001) Rapid development and plasticity of layer 2/3 maps in rat barrel cortex in vivo. Neuron 31:305–315.

Thomson AM, West DC, Wang Y, Bannister AP (2002) Synaptic connections and small circuits involving excitatory and inhibitory neurons in layers 2–5 of adult rat and cat neocortex: triple intracellular recordings and biocytin labelling in vitro. Cereb Cortex 12:936–953.

Tsai PS, Nishimura N, Yoder EJ, White A, Dolnick E, Kleinfeld D (2002) Principles, design and construction of a two photon scanning microscope for in vitro and in vivo studies. In: Methods for in vivo optical imaging (Frostig R, ed), pp 113–171. Boca Raton, FL: CRC.

Uttley AM (1955) The probability of neural connexions. Proc R Soc Lond B Biol Sci 144:229–240.

van Kan PL, Scobey RP, Gabor AJ (1985) Response covariance in cat visual cortex. Exp Brain Res 60:559–563.

Woolsey TA, Van der Loos H (1970) The structural organization of layer IV in the somatosensory region (S1) of mouse cerebral cortex. Brain Res 17:205–242.

Zohary E, Shadlen MN, Newsome WT (1994) Correlated neuronal discharge rate and its implications for psychophysical performance. Nature 370:140–143.